Chirality

Deutsche Ausgabe: DOI: 10.1002/ange.201507502
Internationale Ausgabe: DOI: 10.1002/anie.201507502

Optically Active Nanostructured ZnO Films

*Yingying Duan, Lu Han, Jialiang Zhang, Shunsuke Asahina, Zhehao Huang, Lin Shi, Bo Wang, Yuanyuan Cao, Yuan Yao, Liguo Ma, Cui Wang, Rina K. Dukor, Lu Sun, Chun Jiang, Zhiyong Tang, Laurence A. Nafie, and Shunai Che**

Abstract: *Inorganic nanomaterials endowed with hierarchical chirality could open new horizons in physical theory and applications because of their fascinating properties. Here, we report chiral ZnO films coated on quartz substrates with a hierarchical nanostructure ranging from atomic to micrometer scale. Three levels of hierarchical chirality exist in the ZnO films: helical ZnO crystalline structures that form primary helically coiled nanoplates, secondary helical stacking of these nanoplates, and tertiary nanoscale circinate aggregates formed by several stacked nanoplates. These films exhibited optical activity (OA) at 380 nm and in the range of 200–800 nm and created circularly polarized luminescence centered at 510 nm and Raman OA at 50–1400 cm^{-1}, which was attributed to electronic transitions, scattering, photoluminescent emission, and Raman scattering in a dissymmetric electric field. The unprecedented strong OA could be attributed to multiple light scattering and absorption-enhanced light harvesting in the hierarchical structures.*

Optical activity (OA), as an essential attribute of chiral materials, makes possible their use in many unique biological,[1] mechanical,[2] electronic,[3] magnetic,[4] and optical[5] applications. Chiral materials with OA are common in both nature and manufacturing. Organic materials are usually limited by their relatively poor intrinsic properties, whereas natural inorganic crystals always exhibit refraction-based OA without prominent intensities. There is a pressing need for new inorganic materials with chiral structures that are able to support more efficiently technologies in a variety of fields, such as imaging, optical data storage, and optical communications based on their strong interactions with light. To address this challenge, several chiral inorganic films have been fabricated using engineered glancing-angle deposition[6] and sculpturing[7] as well as duplication in nanocrystalline cellulose.[8] These techniques are limited to either microwave or scattering-based OA. Although many inorganic chiral structure[9] and biomimetic exquisitely complex functional materials[10] incorporating nano-, meso-, and microscale features have been reported, these structures are still far from being practical in chiral films.

In this work, we deposited chiral ZnO nanostructures on a quartz substrate by a facile amino acid-induced self-assembly strategy (see Figure S1 in the Supporting Information).[11] The substrate was activated by simple potassium permanganate solution treatment that forms Mn-(hydroxy)-oxide deposits on the surface that act as an efficient seed layer that allows the growth of hydroxide zinc carbonate (HZC) by chemical bath deposition.[12] The chiral HZC nanostructures were deposited on the activated quartz substrate from a homogeneous solution composed of methionine, zinc salt, ammonium carbonate, and deionized water under hydrothermal conditions. The L/D-methionine was selected as both the structure-directing agent and the symmetry-breaking agent for the asymmetric attachment and co-self-assembly process with Zn^{2+} ions because of their coordinative bonding behavior.[13] The ammonium carbonate hydrolyzed fast and produced many OH^- in a short period; the Zn^{2+} ions in solution would precipitate out rapidly because of the high pH environment and subsequently grow HZC.[14] The chiral ZnO nanoparticles arrayed on the substrate could be obtained by calcination of HZC. The chiral nanostructured ZnO films (CNZFs) and chiral nanostructured ZnO powders (CNZPs) were collected by simply removing the quartz wafer and followed by centrifugation of the precipitate from the synthesis solution.

Figure 1a and b presents scanning electron microscopy (SEM) images of CNZFs with different distribution densities synthesized using L-methionine as the structure-directing agent and zinc acetate hydroxide as the zinc source. The density of the chiral ZnO nanostructures on the substrate was

[*] Y. Duan,[+] L. Han,[+] J. Zhang,[+] Z. Huang, Y. Cao, Y. Yao, L. Ma, C. Wang, Prof. S. Che
School of Chemistry and Chemical Engineering
State Key Laboratory of Metal Matrix Composites
Shanghai Jiao Tong University
800 Dongchuan Road, Shanghai, 200240 (P.R. China)
E-mail: chesa@sjtu.edu.cn
Homepage: http://che.sjtu.edu.cn
Dr. S. Asahina
SMBU, JEOL, Akishima, Tokyo 196-8558 (Japan)
L. Shi, Prof. Z. Tang
Key Laboratory of Nanosystem and Hierarchical Fabrication
Chinese Academy of Sciences
National Center for Nanoscience and Technology
No.11, Beiyitiao, Zhongguancun, Beijing, 100190 (P. R. China)
B. Wang, R. K. Dukor, Prof. L. A. Nafie
BioTools, Inc.
17546 Bee Line Hwy, Jupiter, FL, 33458 (USA)
Prof. L. A. Nafie
Department of Chemistry, Syracuse University
Syracuse, NY, 13244 (USA)
L. Sun, Prof. C. Jiang
School of Electronic Information and Electrical Engineering, State Key Laboratory of Advanced Optical Communication System and Network, Shanghai Jiao Tong University
800 Dongchuan Road, Shanghai, 200240 (P.R. China)
[+] These authors contributed equally to this work.

Supporting information for this article is available on the WWW under http://dx.doi.org/10.1002/anie.201507502.

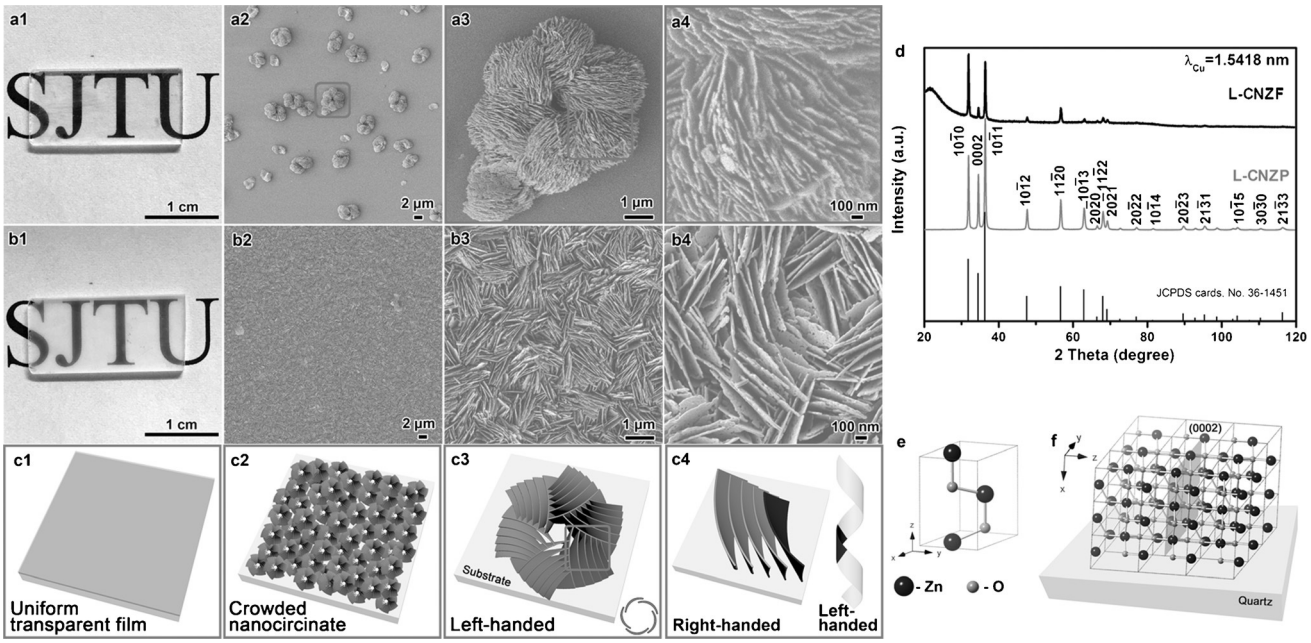

Figure 1. a1–a4) SEM images at varying magnifications of sparse L-CNZF, b1–b4) dense L-CNZF and c1–c4) a schematic drawing of the hierarchical chirality in L-CNZFs. d) The XRD patterns of dense L-CNZF and L-CNZP centrifuged from the same autoclave as CNZF. e) The crystal structure and f) growing direction of the ZnO nanoplates along the substrate. The synthetic molar composition was 1.0 L-methionine:1.5 $Zn(CH_3OO)_2$:0.5 $(NH_3)_2CO_3$:1389 H_2O.

controlled by adjusting the activation degree with different concentrations of $KMnO_4$ and different activation times. As shown in Figure 1 a1–4, the sparse CNZF synthesized on the quartz substrate activated with a low $KMnO_4$ concentration of 0.04 mM was composed of particles with a circinate helical morphology, which consists of several dozens of bended nanoplates in a counterclockwise manner defined as sinistrorse or left-handed asymmetry (denoted L-CNZF; Figure 1 a3 and c3). Although it is difficult to determine the morphology and handedness of nanoplates using SEM images because of their slight bending degree, the exclusive right-handed stacking of the nanoplates can be observed in Figure 1 a4. Based on the bending direction of the nanoplates, the right-handed stacking originates from the left-handed chiral morphology of the nanoplates (Figure 1 c4). The nanoplates of L-CNZF were confirmed to be short segments of helically coiled ribbons by electron microscopy. Therefore, in the presence of L-methionine, the primary left-handed ZnO coiled nanoplates were helically stacked in the secondary right-handed form, which forms a left-handed tertiary circinate helical morphology. The circinate ZnO nanoparticles formed with D-methionine exhibited the same structure in the opposite direction, that is, right-handed CNZF (R-CNZF; Figure S2).

When the substrate surface was treated with a high $KMnO_4$ concentration (10 mM), the resulting large number of activation sites made possible the growth of HZC and the production of high-density ZnO nanoparticles. As shown in Figure 1 b1–4, the transparent L-CNZF with a smooth and uniform surface was composed of dozens of compactly arrayed bended nanoplates with lengths of 0.5–1.5 μm, thicknesses of about 20 nm, and heights of about 1.5 μm (Figure S3) grown almost vertically from the surface of the substrate in an interval space of 50–200 nm. Although non-clear chiral morphologies and structures similar to the circinate aggregates shown in sparse CNZFs were observed, small amounts of nanoscale circinate aggregates still existed, implying that the dense CNZFs showing three levels of chirality were formed with the crowded nanoscale circinate aggregates.

The crystalline structure of the CNZFs was analyzed using wide-angle X-ray diffractometry. Figure 1 d shows the XRD patterns of the L-CNZF and L-CNZP shown in Figure 1 b and Figure S4a, respectively. The reflections in the resulting spectrum indicate identical structures of the wurtzite hexagonal phase of ZnO [JCPDS file 36-1451] with the space group $P6_3mc$ and lattice parameters of $a = 3.25$ Å and $c = 5.21$ Å.[15] The intensity of 0002 and some other reflections of the CNZF are much lower than those of CNZP, suggesting that ZnO crystals were parallelly grown along [0002] on the substrate (Figure 1 f). No other peak related to impurities, such as zinc carbonate, zinc hydroxide, was detected.

The intrinsic chiral nature and fine crystalline structure of the ZnO nanoplates has been determined from transmission electron microscopy (TEM), as shown in Figure 2. Figure 2 a–c shows low-magnification TEM images and the corresponding selected area electron diffraction (SAED) patterns of the L-CNZF are depicted in Figure 1 b; they reveal the single-crystal-like structure of the nanoplate. When the SAED pattern in the top part is aligned in the [10-10] direction, the zone axis becomes misaligned in the middle and bottom parts. By tilting the nanoplate along its [10-11] axis by 2.97° and 6.22°, the middle and bottom parts, respectively, become well aligned, indicating that the crystal structure is continuously

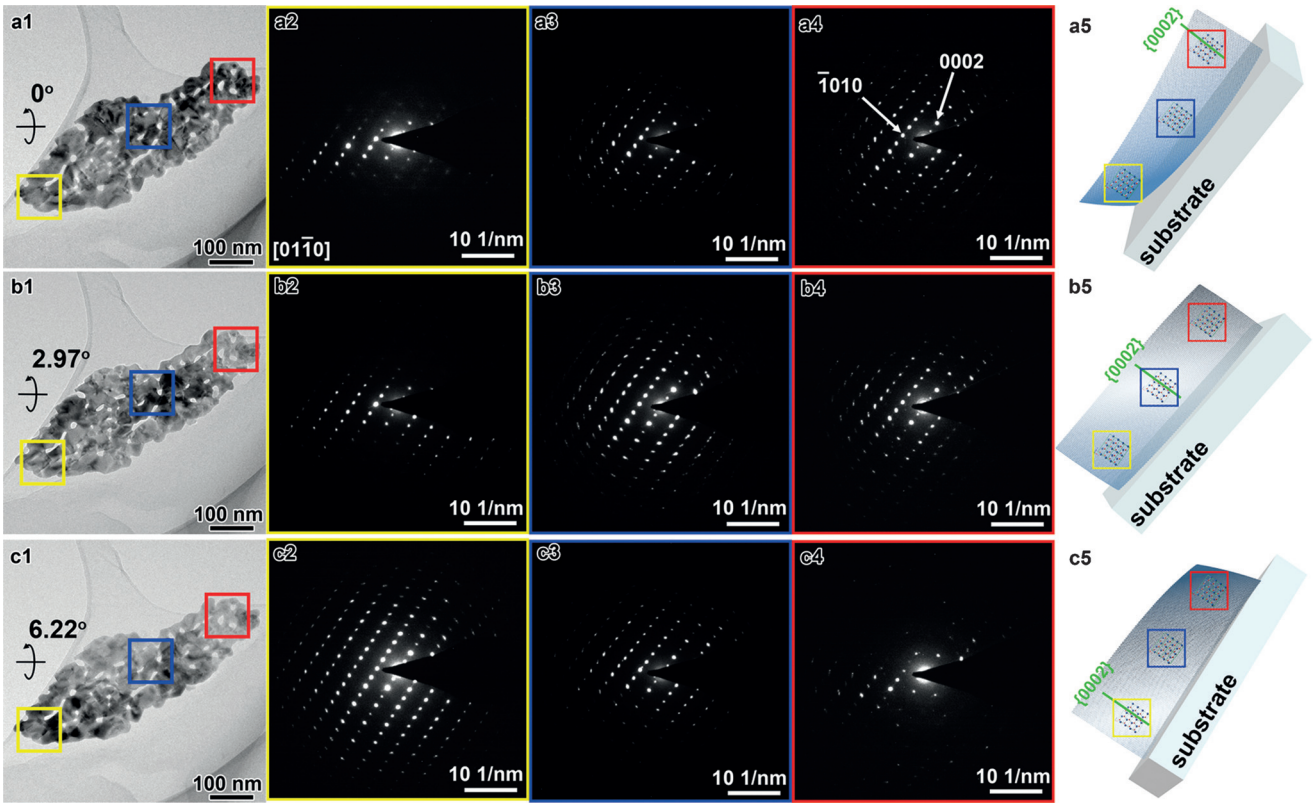

Figure 2. TEM images and corresponding SAED patterns of the nanoplate as well as its schematic structural model of left-handed form. a1–5) The nanoplate is bent, and the [01-10] axis can be aligned only with the incident electron beam from the top region. By tilting the crystal along the [10-11] axis by 2.97° and 6.22°, respectively, b1–5) the middle and c1–5) bottom parts can be aligned.

tilted slightly along its [10-11] axis. The slight bending caused small distortion of the SAED patterns. Based on the XRD results and the above TEM analysis, it can easily be estimated that in the chiral nanoplates a segment of the left-handed coiled ribbon would be grown parallel along [0002] and tilted along [10-11] axis (Figure 2 a5, b5, and c5).

High-resolution transmission electron microscopy (HRTEM) images and corresponding Fourier diffractograms (FDs) of the nanoplates (Figure S5a1-4) reveal the well-resolved lattice fringes of the single-crystalline wurtzite ZnO taken along the [01-10] direction. Notably, the single-crystal shares a similar bend orientation to the entire nanoplate. By taking the FDs from different parts, a small rotational relationship of the reflections can be observed. The reflections rotate counterclockwise from the top to the bottom, indicating a coiled distortion of the crystal structure (Figure S5 b1–4). These results indicate that the helically coiled nanoplates are formed by the helical distortion of ZnO single crystals. Based on the tilting angle and corresponding distance, the pitch length was calculated to be as long as 30 μm. The crystal forming the nanoplate would be helically distorted with a very subtle left-handed malposition along the [10-11] axis (Figure S5b1).

An oriented distortion of the ZnO crystal could be induced by the chiral center of the methionine molecules through coordination bonding (Figure S6), which would force the ZnO crystal to form some lattice defects. Because the ZnO $P6_3mc$ structure prefers to form a flat morphology, its crystal structure cannot accommodate a large tortuous angle, resulting in fracture and deflected crack holes (Figure S7), but the single crystal still coiled with a very subtle distortion along [10-11] axis might because of the lower surface energy of the {10-11} plane.[16] This behavior makes the nanoplate more prone to coiling, and subsequent stacking leads to the circinate helical architecture.

Materials with definite spatial orientations will interact preferentially with polarized electromagnetic waves, leading to the phenomenon of OA. The different OAs originate from the different scales of chirality. The chiral distorted crystalline structure and helically aggregated nanounits that are smaller than the Bohr radius[17] cause a dynamic Coulomb interaction in a dissymmetric field electron transition from the valence band to the conduction band of ZnO,[15] and vice versa.[18] This results in electron transition-based and emission-based OA on the basis of structural considerations.[9b,19] Similarly, vibrational absorption-based OA will be generated in the infrared and far-infrared regions. The circular dichroism (CD) reflects the OA and molecular conformation in the electronic ground state, whereas circularly polarized luminescence (CPL) reflects OA in the electronic excited state involved in the emission process (S_1 for fluorescence) and Raman OA (ROA) provides vibrational dissymmetry information.[18] These behaviors occur because the chiral centers exist in dissymmetric environments in the transitions of electronic

and vibrational states.[17,20] Consequently, the absorption-, vibration-, and emission-based OAs originate only from the primary crystalline chirality of the CNZFs and are impossible from micrometer-scaled secondary and tertiary chirality. A medium with left-handed helical structure absorbs right-handed circularly polarized light and exhibits exciton coupling signals changing from negative to positive with shortened wavelength. The left-handed helical structure prefers to emit left-handed circularly polarized light and display a positive CPL signal.[20]

The helically stacked nanoplates beget the chiral morphology of the ZnO nanostructures, and the chiral morphology begets the chiral interface between two media with different permittivities (ZnO and air here), resulting in selective reflection of one-handedness of circularly polarized light and transmission of the other handedness, which could contribute to scattering-based OA.[1a,6b,8a,b,21] A medium with a right-handed helical structure reflects right-handed circularly polarized light.[22] Therefore, the three chirality levels of the CNZFs are all able to produce scattering-based OAs on the electromagnetic wavelength scale.

First, the OA was detected using transmitted UV/Vis and CD spectroscopy (Figure 3 a1). Experimental mirror-imaged CD spectra were obtained for antipodal dense CNZFs. The transmitted CD spectra of L- and R-CNZFs on the quartz wafer exhibited signals that were so strong that they exceeded the acceptable range of the instrument. As shown in the schematic illustration (Figure 3 a2), the transmitted CD signals include both absorption-based parts and scattering-based parts [$CD=(A_L-A_R)+(S_L-S_R)$].

To discriminate between these two parts and separate out absorption-based OAs, the CNZFs were further examined by addition of water (isotropic liquid). After infiltration with water, the scattering-based OA weakened dramatically (Figure 3 b1) because the optical chiral morphology disappeared with decreasing difference between optical refractive indices of two materials (ZnO and air, ZnO and water).[6b,8a] A sharp peak centered at 380 nm corresponding to the characteristic absorption band of ZnO was observed. Because the refractive indices of water ($n=1.33$) and ZnO ($n=1.9$) are not perfectly matched, a small residual scattering-based OA is expected and another sharp couplet of absorption-based OA is not

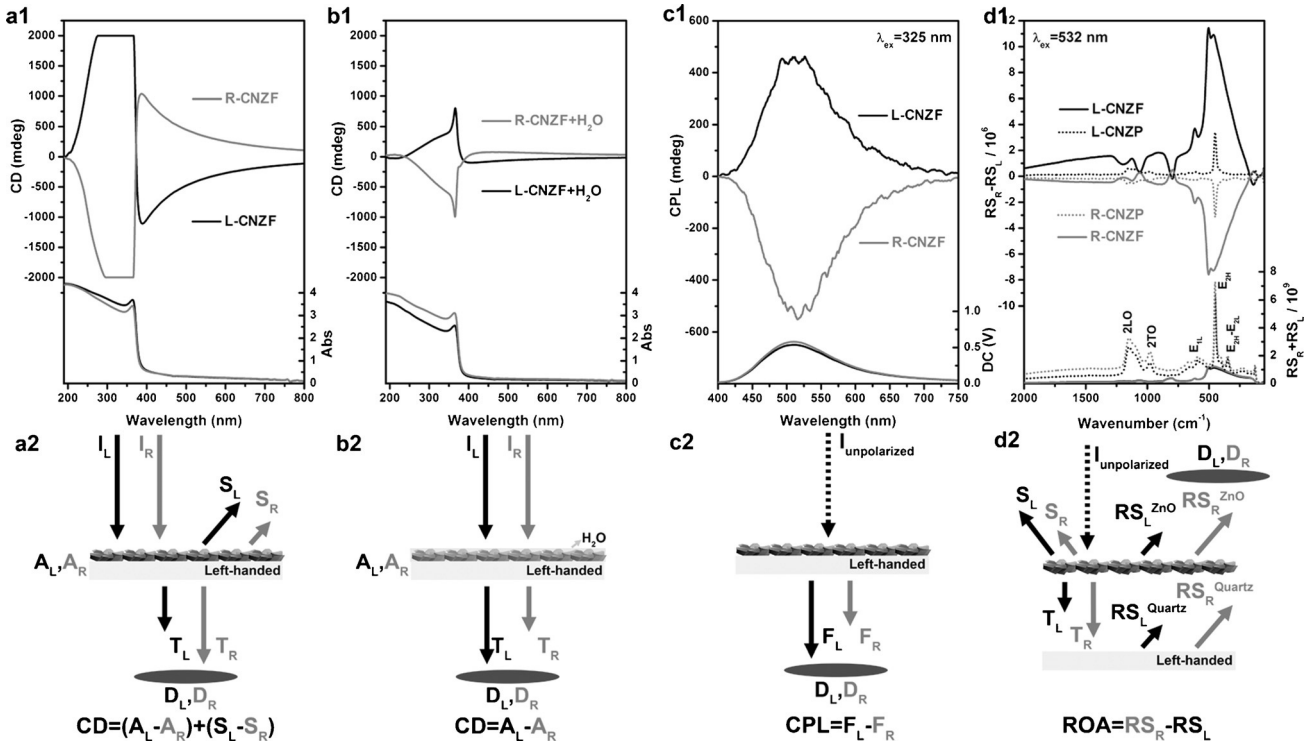

Figure 3. Transmitted UV/Vis and CD spectra and schematic illustration of a) the antipodal dense CNZFs formed with L/D-methionine and b) the antipodal dense CNZFs infiltrated with water, indicating the electron transition- and scattering-based OAs. c) PL and CPL spectra at an excitation wavelength of 325 nm, indicating the emission-based OA. d) SCP ROA of the antipodal CNZFs (solid lines) and CNZPs (dashed lines). I is the incident light ($I_L=I_R$), A is the absorbed light, T is the transmitted light, S is the scattered light, D is the detected light, F is the fluorescent light and RS is Raman scattered light. According to the characteristic mechanism, the detected signal for transmitted light is D=T, and transmitted $CD=(I_L-D_L)-(I_R-D_R)=(I_L-T_L)-(I_R-T_R)=[I_L-(I_L-S_L-A_L)]-[I_R-(I_R-S_R-A_R)]=(S_L+A_L)-(S_R+A_R)=(A_L-A_R)+(S_L-S_R)$; after infiltration with water, the reflection arising from the Bragg resonance disappeared and I=A+T, the $CD=(I_L-D_L)-(I_R-D_R)=(I_L-T_L)-(I_R-T_R)=A_L-A_R$; the detector signal for CPL is D=F, and $CPL=F_L-F_R$; in SCP ROA, the Raman-scattered light (RS) were detected, SCP $ROA=RS_R-RS_L$. When incident light (532 nm) reached the ZnO film first, the left-handed circularly polarized light (532 nm) would be selectively scattered by the left-handed structure of the ZnO film based on Bragg resonance reflection. At the same time, selective Raman scattering occurred with other wavelengths from chiral ZnO. On the other hand, right-handed circularly polarized light (532 nm) transmitted more than left-handed, which enhanced selectively Raman scattering with other wavelengths by induced chiral quartz. Thus quartz exhibit so high ROA intensities by which the ROA of ZnO is not obvious.

obvious. Therefore, for the L-CNZF, it can be considered that the scattering-based CD signals changed from negative in the range of 400–800 nm to positive in the range of 200–400 nm (Figure S8), indicating that this film reflected right-handed circularly polarized light at long wavelengths and left-handed circularly polarized light at short wavelengths. In transmission CD measurement, the negative and positive scattering-based OA peaks originate from the right-handed stacking nanoplates and left-handed coiled nanoplates, respectively. The absorption-based negative couplet CD signals at 380 nm overlap with scattering-based OA in the range of 200–400 nm. The results were confirmed by the as-synthesized chiral HZC films (Figure S9). Furthermore, remarkably strong intensities of CD peaks in the range of 200–400 nm might attribute to multiple light scattering and absorption-enhanced light harvesting in the hierarchical structures.

Figure 3c1 shows the photoluminescence (PL) and CPL spectra of antipodal CNZFs. The CNZFs exhibit CPL centered at 510 nm corresponding to the PL, with CPL values of 500 mdeg at an excitation wavelength of $\lambda_{ex} = 325$ nm, which is consistent with the fluorescence maximum. It has been suggested that the green emission band corresponds to the singly ionized oxygen vacancy in ZnO and results from the recombination of a photogenerated hole with the single ionized charge state of this defect.[18] The positive CPL signal from the L-CNZF confirms that the primary chirality of the nanoplates is in the left-handed form.[20]

The chirality of CNZFs in angstrom scale was unambiguously detected by ROA with scattered circular polarization (SCP) measurement strategy in this work. The dashed lines in Figure 3d1 show the ROA of antipodal CNZPs. All observed peaks can be assigned to a wurzite ZnO structure.[15] The presence of a high intensity, sharp and dominated E_2 and other weak modes showing mirror images in the SCP ROA spectra indicates that the antipodal CNZPs are highly crystalline with opposite chirality. However, the Raman and ROA spectra of CNZFs (solid lines in Figure 3d1) exhibit the counterparts of TO-LO pairs in vitreous SiO_2.[23] It can be presumed that the ROA of quartz was induced in the interface and amplified by the CNZFs, which is so strong that the ROA of the CNZFs is buried. The ROA amplification of quartz can be explained in terms of the behavior of the interaction between light and media. The incident light is selectively transmitted by the CNZFs and Raman scattered by quartz resulting in enhanced opposite ROA signals of achiral quartz coated with antipodal CNZFs.

It can be concluded that three levels of hierarchical chirality exist in the CNZFs. Using L-CNZF as an example, the three levels of chirality can be described as follows: 1) the highest tertiary chirality has a circinate architecture with a defined sinistrorse or left-handed asymmetry (Figure 1c3); 2) the secondary chirality consists of right-handed chiral stacking of nanoplates (Figure 1c4) and is responsible for the scattering-based OA in the range from 400 to 800 nm; and 3) the primary chirality originates from left-handed chiral nanoplates that stretch like a coiled ribbon and arises from the distorted single crystals (Figure 1c4 and Figure S5b). This primary chirality produces absorption- and scattering-based OAs in the range of 200–400 nm, the CPL centered at 510 nm and the SCP ROA range from 50–1400 cm^{-1}.

In summary, chiral ZnO thin films with hierarchical chiral structures, including atomic, nano-, meso-, and microscales, were synthesized for the first time by self-assembly of a symmetry-breaking chiral molecule and an inorganic source, which might contribute to comprehensive understanding of biomineralization. To the best of our knowledge, this is the first example of chiral inorganic films that exhibits multiple OAs, such as prominent electron transition-based OA, scattering-based OA, CPL, and ROA simultaneously. These remarkably high CD, CPL, and ROA dissymmetry might attribute to multiple light scattering and absorption-enhanced light harvesting in the hierarchical chiral structures, which are in accordance with natural biomaterials. These solid-state nanomaterials with multiple OAs over a large range of wavelengths with strong intensities and high CPL, ROA dissymmetry demonstrate the potential of ZnO for future device applications in optics, optoelectronics, sensors, actuators, energy applications, spintronics, and other areas.

Acknowledgements

This work was supported by the National Natural Science Foundation (grant numbers 21471099 and 21201120), the National Basic Research Program (grant number 2013CB934101) of China and A Foundation for the Author of National Excellent Doctoral Dissertation of China (201454). We thank the Instrumental Analysis Centre of Shanghai Jiaotong University for CD measurements.

Keywords: chirality · circular dichroism · inorganic films · luminescence · Raman optical activity

How to cite: *Angew. Chem. Int. Ed.* **2015**, *54*, 15170–15175
Angew. Chem. **2015**, *127*, 15385–15390

[1] a) V. Sharma, M. Crne, J. O. Park, M. Srinivasarao, *Science* **2009**, *325*, 449–451; b) S. Vignolini, P. J. Rudall, A. V. Rowland, A. Reed, E. Moyroud, R. B. Faden, J. J. Baumberg, B. J. Glover, U. Steiner, *Proc. Natl. Acad. Sci. USA* **2012**, *109*, 15712–15715.
[2] Z. Xu, C. Gao, *Nat. Commun.* **2011**, *2*, 571.
[3] a) D. J. Broer, J. Lub, G. N. Mol, *Nature* **1995**, *378*, 467–469; b) R. A. M. Hikmet, H. Kemperman, *Nature* **1998**, *392*, 476–479; c) T. Yoshioka, T. Ogata, T. Nonaka, M. Moritsugu, S. N. Kim, S. Kurihara, *Adv. Mater.* **2005**, *17*, 1226–1229.
[4] a) G. H. Glover, C. E. Hayes, N. J. Pelc, W. A. Edelstein, O. M. Mueller, H. R. Hart, C. J. Hardy, M. O'Donnell, W. D. Barber, *J. Magn. Reson.* **1985**, *64*, 255–270; b) A. Rogacheva, V. Fedotov, A. Schwanecke, N. Zheludev, *Phys. Rev. Lett.* **2006**, *97*, 177401.
[5] a) J. Pendry, *Science* **2004**, *306*, 1353–1355; b) J. K. Gansel, M. Thiel, M. S. Rill, M. Decker, K. Bade, V. Saile, G. Von Freymann, S. Linden, M. Wegener, *Science* **2009**, *325*, 1513–1515; c) M. H. Song, N. Y. Ha, K. Amemiya, B. Park, Y. Takanishi, K. Ishikawa, J. W. Wu, S. Nishimura, T. Toyooka, H. Takezoe, *Adv. Mater.* **2006**, *18*, 193–197.
[6] a) N. O. Young, J. Kowal, *Nature* **1959**, *183*, 104–105; b) K. Robbie, D. J. Broer, M. J. Brett, *Nature* **1999**, *399*, 764–766.
[7] a) Q. Wu, I. J. Hodgkinson, A. Lakhtakia, *Opt. Eng.* **2000**, *39*, 1863–1868; b) M. Decker, M. W. Klein, M. Wegener, S. Linden, *Opt. Lett.* **2007**, *32*, 856–858; c) K. Konishi, M. Nomura, N.

Kumagai, S. Iwamoto, Y. Arakawa, M. Kuwata-Gonokami, *Phys. Rev. Lett.* **2011**, *106*, 057402.
[8] a) K. E. Shopsowitz, H. Qi, W. Y. Hamad, M. J. MacLachlan, *Nature* **2010**, *468*, 422 – 425; b) K. E. Shopsowitz, A. Stahl, W. Y. Hamad, M. J. MacLachlan, *Angew. Chem. Int. Ed.* **2012**, *51*, 6886 – 6890; *Angew. Chem.* **2012**, *124*, 6992 – 6996; c) K. E. Shopsowitz, W. Y. Hamad, M. J. MacLachlan, *Angew. Chem. Int. Ed.* **2011**, *50*, 10991 – 10995; *Angew. Chem.* **2011**, *123*, 11183 – 11187.
[9] a) B. Liu, L. Han, S. Che, *Angew. Chem. Int. Ed.* **2012**, *51*, 923 – 927; *Angew. Chem.* **2012**, *124*, 947 – 951; b) Y. Duan, X. Liu, L. Han, S. Asahina, D. Xu, Y. Cao, Y. Yao, S. Che, *J. Am. Chem. Soc.* **2014**, *136*, 7193 – 7196.
[10] a) T. Sugawara, Y. Suwa, K. Ohkawa, H. Yamamoto, *Macromol. Rapid Commun.* **2003**, *24*, 847 – 851; b) C. A. Orme, A. Noy, A. Wierzbicki, M. T. McBride, M. Grantham, H. H. Teng, P. M. Dove, J. J. DeYoreo, *Nature* **2001**, *411*, 775 – 779; c) F. Wang, B. Cao, C. Mao, *Chem. Mater.* **2010**, *22*, 3630 – 3636.
[11] C. Yan, D. Xue, *J. Phys. Chem. B* **2006**, *110*, 11076 – 11080.
[12] M. Kokotov, G. Hodes, *J. Mater. Chem.* **2009**, *19*, 3847 – 3854.
[13] Q. D. Truong, T. H. Le, T. Kimura, S. Yin, T. Sato, Y.-C. Ling, *RSC Adv.* **2013**, *3*, 19154 – 19160.
[14] T. Baird, K. C. Campbell, P. J. Holliman, R. W. Hoyle, D. Stirling, B. P. Williams, M. Morris, *J. Mater. Chem.* **1997**, *7*, 319 – 330.
[15] Ü. Özgür, Y. I. Alivov, C. Liu, A. Teke, M. Reshchikov, S. Doğan, V. Avrutin, S.-J. Cho, H. Morkoc, *J. Appl. Phys.* **2005**, *98*, 041301.
[16] Q. Ahsanulhaq, A. Umar, Y. B. Hahn, *Nanotechnology* **2007**, *18*, 115603.
[17] D. Keller, C. Bustamante, *J. Chem. Phys.* **1986**, *84*, 2972 – 2980.
[18] S. Xu, Z. L. Wang, *Nano Res.* **2011**, *4*, 1013 – 1098.
[19] S. Liu, L. Han, Y. Duan, S. Asahina, O. Terasaki, Y. Cao, B. Liu, L. Ma, J. Zhang, S. Che, *Nat. Commun.* **2012**, *3*, 1215.
[20] J. Liu, H. Su, L. Meng, Y. Zhao, C. Deng, J. C. Y. Ng, P. Lu, M. Faisal, J. W. Y. Lam, X. Huang, H. Wu, K. S. Wong, B. Z. Tang, *Chem. Sci.* **2012**, *3*, 2737 – 2747.
[21] B. Liu, L. Han, Y. Duan, Y. Cao, J. Feng, Y. Yao, S. Che, *Sci. Rep.* **2014**, *4*, 4866.
[22] F. Livolant, M. F. Maestre, *Biochemistry* **1988**, *27*, 3056 – 3068.
[23] B. Li, D. Yu, S.-L. Zhang, *Phys. Rev. B* **1999**, *59*, 1645.

Received: August 12, 2015
Published online: October 22, 2015

